Environmental Science Advances

ROYAL SOCIETY OF CHEMISTRY

PAPER

View Article Online
View Journal

Check for updates

Cite this: DOI: 10.1039/d5va00243e

Interaction of ADONA with neutral and charged clay interfaces: molecular insights

Christina E. Schumm, Narasimhan Loganathan, James Hager and Angela K. Wilson *

Ether-based per- and polyfluorinated alkyl substances (PFAS) are increasingly used as alternatives to legacy PFAS due to their higher tendency to break down in natural settings. Among these, ADONA – a carboxylate ether-PFAS replacement species – is a prominent substitute for PFOA. However, despite its intended decrease in toxicological behavior, ADONA has been associated with some adverse effects in biological systems and is considered an emerging contaminant. Subsequent to employing ADONA for nearly two decades, these molecules are increasingly detected in environmental matrices, particularly near industrial sites. Consequently, there is an increased risk for human exposure through water sources. At the same time, soil minerals could play a central role in governing the leaching of ADONA from surface environments to groundwater. In this study, the influence of soil mineral components on the distribution and transport of ADONA in terrestrial environments has been investigated using molecular dynamics (MD) simulations. Three common clay minerals were chosen as models due to their distinct variations in both charge distribution and magnitude at their basal surfaces. The interfacial adsorption structures and dynamic properties of ADONA vary substantially between different mineral surfaces, and the adsorption mechanism strongly depends on the surface charge of the minerals examined.

Received 31st July 2025
Accepted 12th October 2025

DOI: 10.1039/d5va00243e

rsc.li/esadvances

Environmental significance

Ether based PFAS are considered as potential alternatives for legacy PFAS molecules and are envisioned to be less bio-accumulative in nature. With increasing studies showing health impacts following exposure to ether PFAS molecules, it is imperative to understand their different exposure pathways to humans. Soils and sediments represent important mediums for exposure among others and play a critical role in determining the movement of alternatives to groundwater. The current study provides a comprehensive knowledge into the interfacial behavior of ADONA, an ether based PFAS molecule at the confined pores of three different soil minerals. The study reveals key interaction that governs the adsorption and dynamics of ADONA varies between minerals. Such insights could be useful when assessing their environmental distribution.

Introduction

Per- and polyfluoroalkyl substances (PFAS), a group of anthropogenic organic compounds including over ~14 000 species, are known for their high persistence and toxicological behavior within environmental and biological systems.[1–4] Though these molecules were first developed in the late 1930's, PFAS have only recently been classified as emerging contaminants and linked to numerous notable health concerns.[5–8] Among the most widely known PFAS are perfluorocarboxylic acids (PFCAs) and perfluorosulfonic acids (PFSAs), which were originally synthesized because of their desirable amphiphilic properties.[9,10] The composition of the molecular backbone includes multiple carbon-fluorine bonds – each with a bond dissociation energy of ~116 kcal mol^{-1} – that account for the exceptional stability of PFAS and their resistance to natural degradation processes such as photochemical oxidation and biodegradation.[11–14] Consequently, it is these same structural features that also contribute to the high persistence of PFAS in the environment and their potential to bioaccumulate, even at trace concentrations.[15–18]

In response to the growing concerns about the adverse environmental and human health effects of PFAS, regulatory measures are now established for legacy PFAS. As well, for some PFAS, rigorous efforts have been introduced to identify safer alternatives for PFAS that can exhibit similar amphiphilic properties. For example, perfluoroalkyl ether acids (ether-PFAS) are a subset of "new age" PFAS alternatives that include at least one alkyl-ether linkage.[19,20] Ether linkages can disrupt the stability of the compound and decrease potential toxicological effects compared to their long-chain perfluorinated analogues.[21,24] Common alternatives for PFOA are hexafluoropropylene oxide dimer acid (HFPO-DA, GenX) and 4,8-dioxa-3*H*-perfluorononanoic acid (ADONA). While studies have shown that ADONA may be less toxic than conventional PFAS compounds such as PFOA, ether-PFAS have recently emerged as

Department of Chemistry, The MSU Center for PFAS Research, Michigan State University, East Lansing, Michigan 48824, USA. E-mail: akwilson@msu.edu

Open Access Article. Published on 13 October 2025. Downloaded on 10/26/2025 4:29:19 AM. This article is licensed under a Creative Commons Attribution-NonCommercial 3.0 Unported Licence.

Open Access Article. Published on 13 October 2025. Downloaded on 10/26/2025 4:29:19 AM. This article is licensed under a Creative Commons Attribution-NonCommercial 3.0 Unported Licence.

a distinct class of concern due to their environmental persistence and potential for bioaccumulation. Some evidence suggests that certain ether-PFAS may preferentially accumulate in specific organs, such as the liver, raising new questions about their long-term biological impacts.[22,23]

ADONA was introduced in the late 2000's and is primarily used as a processing aid in fluoropolymer production, but also is included in applications for the manufacturing of non-stick coatings and electronic components.[24–27] With declining legacy PFAS concentrations near industrial sites, detectable levels of ADONA in nearby groundwater have been reported.[31] However, as noted in the study, the associated health risks may be relatively low, due to ADONA's shorter half-life as compared to that of long-chain PFAS. Nonetheless, ADONA concentrations, particularly in ground and surface waters near industrial facilities, are on the rise.[28–30] Furthermore, ADONA has been detected in human plasma and breast milk and may be linked to adverse birth outcomes.[31,32] Understanding ADONA's behavior in environmental media such as water, soil, and sediments is therefore critical, as these systems serve as both direct and indirect exposure pathways for humans, animals, and plants.[33]

According to Feng *et al.*, ether-PFAS have the potential for long-range transport in the atmosphere, aquatic and soil environments, much like other well-known PFAS compounds.[23] Particularly, ADONA has been detected in agricultural soils in both Germany and China, with sources linked to paper sludge and compost application or nearby industrial discharge.[34–36] These soils contaminated with ADONA pose a risk of transportation of ADONA to groundwater *via* leaching.[34–36] ADONA transport is likely to follow similar environmental pathways as legacy PFAS.[16,17] While current research has largely focused on the aqueous phase transport of ADONA, there is a gap in knowledge about the role that soil components – particularly clay minerals (a major soil fraction) – have in influencing its retention and mobility.[37–39] Clay minerals, which vary in their surface charge characteristics, play a pivotal role in the interfacial properties of PFAS at a molecular level.[18,38,40,41] However, the behavior of ADONA in clay minerals is largely unexamined – despite its importance for informing regulatory processes and developing effective remediation strategies.

In the present study, the adsorption mechanisms of ADONA in three representative clay minerals – kaolinite, montmorillonite, and illite – are investigated. These clays were chosen because they vary greatly in their charge magnitude and distribution and represent a wide variety of typical clay types in soils. Kaolinite is a neutral clay exhibiting two unique basal surfaces exposed to the mesopore region-a hydrophobic siloxane (octahedral) surface and a hydrophilic hydroxyl surface (tetrahedral) surface. Montmorillonite has a relatively low structural charge due to a moderate distribution of substituted sites in both tetrahedral and octahedral layers, while illite has a high structural charge which is distributed exclusively in the tetrahedral layers. In this work, classical molecular dynamics simulations have been used to examine the adsorption behavior, coordination structure, and diffusion characteristics of ADONA for each of these clays. To date, the interactions of ADONA with these clay structures have not been directly examined.

Simulation details

The structural composition of kaolinite, $Al_4Si_4O_{10}(OH)_8$, is based on the model from Cygan *et al.*[42] The montmorillonite structural formula, $M^+(Si_{7.25}Al_{0.25})(Al_{3.25}Mg_{0.75})O_{20}(OH)_4$, follows the model described by Ngouana and Kalinichev.[43] Isomorphic substitutions of Al^{3+}/Si^{4+} in the tetrahedral sheets and the Mg^{2+}/Al^{3+} in the octahedral layer result in a charge of $-0.75|e|$ per unit cell. Hydrated Ca^{2+} counterions were distributed in the smectite's swellable interlayer. Illite is represented by the structural formula of $M^+(Si_{6.4}Al_{1.6})(Al_4)O_{20}(OH)_4$ and is derived from an ideal muscovite structure, with a 20% reduction in substituted Al^{3+}.[44] The Al^{3+}/Si^{4+} isomorphic substitutions in the tetrahedral sheets result in a charge of $-1.6|e|$ per unit cell that is balanced by K^+ counterions in the non-swellable interlayer. All isomorphic substitutions for montmorillonite and illite were made in a quasi-disordered manner obeying Löwenstein's avoidance rule, which prohibits Mg–O–Mg or Al–O–Al linkages.[45] Each clay model was chosen based on its capabilities to accurately reproduce the interfacial structure and dynamical properties of metal ions and organics, consistent with experimental studies.[46–50] The structural differences between the three minerals are illustrated in Fig. S2.

Clay surfaces were constructed by cleaving the center of each interlayer along the crystallographic (001) plane and adding a ~130 Å mesopore to effectively minimize any interactions of one surface with another from neighboring cells. The clay structures were expanded into a (12 × 8 × 2) supercell, with a large basal surface. Each simulation system included two clay layers (~62 × ~72 Å laterally) and the initial dimensions are described in Table S1. The interparticle mesopores were hydrated with ~20 000 H_2O molecules under ambient conditions ($P = 1$ atm and $T = 300$ K). The initial models included 16 ADONA molecules randomly distributed within the mesopore into four regions with each region separated by ~20 Å, as represented in Fig. S3. In addition, ADONA molecules within a given region were placed ~15–20 Å from one another. To model neutral pH conditions, all terminal carboxyl groups on ADONA were deprotonated, resulting in $C_7HF_{12}O_4^-$ anions. The number of ADONA molecules per simulation was chosen to mimic concentrations at soil sites reported to have high levels of contamination in the range of ppm, similar to concentrations for both legacy and other emerging PFAS alternatives.[51,52] To maintain charge neutrality, Ca^{2+} counterions were randomly distributed throughout the interparticle mesopore, balancing the charges of the clays and the ADONA anions. The initial placements of ADONA and Ca^{2+} in the mesopore region were chosen to avoid biased aggregation or preferential adsorption onto basal surfaces.

Classical molecular dynamics (MD) simulations were carried out for 55 ns using Large-scale Atomic/Molecular Massively Parallel Simulator (LAMMPS), as depicted in (Fig. 1).[53] Simulations were performed for 15 ns in the isobaric-isothermal ensemble (NPT: constant atom number, pressure, and temperature) at ambient thermodynamic conditions ($P = 1$ atm and $T = 300$ K). The first 10 ns of the NPT simulation were for equilibration followed by 5 ns of a production run for data

© 2025 The Author(s). Published by the Royal Society of Chemistry

Open Access Article. Published on 13 October 2025. Downloaded on 10/26/2025 4:29:19 AM. This article is licensed under a Creative Commons Attribution-NonCommercial 3.0 Unported Licence.

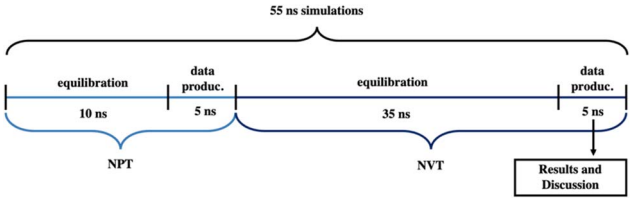

Fig. 1 Timeline for the simulation run.

collection. Subsequently, NVT (constant number of atoms, volume, and temperature) simulations were performed for an additional 40 ns, encompassing another equilibration and data production. The cell dimensions for the NVT simulations were obtained by averaging the results from ten independent 500 ps time blocks (from the NPT data production run – see Table S1). The velocity Verlet integrator was used to calculate the equations of motion with a timestep of 1 fs, with data collected at 10 fs time intervals. Data analysis was based on the final 5 ns of the NVT production run. Three-dimensional periodic boundary conditions were employed to simulate infinite clay particle surfaces. The temperature and pressure were maintained using a Nosé-Hoover barostat (controlled anisotropically) and thermostat.[54,55]

Fully flexible all-atom force fields were used to model the interactions between clay particles, ADONA, and water. Clay and cation interatomic interactions were modelled using revised ClayFF, a generalized amber forcefield (GAFF2), for ADONA and by the single point charge (SPC) interaction potential for water.[42,56,57] The ADONA partial atomic charges were calculated using the AM1-BCC charging method *via* the Antechamber module.[58,59] The selected interaction potentials were chosen for the demonstrated ability to accurately reproduce experimental observations and is widely applied in simulations involving clay surface interactions with both organic or inorganic species.[4,60–64] The short-range, non-electrostatic interactions were calculated using a cutoff of 10 Å, while long-range electrostatic interactions were calculated using particle–particle particle-mesh (PPPM) summation with an accuracy of 1×10^{-6}.[65]

Results and discussion

Atomic density profiles

Atomic density profiles (ADP) were calculated for each clay model to provide insight into how the density of different atomic species change with respect to distance along the clay surface normal (001 plane), shown in Fig. 2. In general, all clay models include ADONA-surface interactions and show varying density distributions for ADONA within the bulk mesopore regions. Descriptions of the density profiles of ADONA, water, and Ca^{2+} for each clay are discussed below, while more specific details about the clay particles are discussed in the SI.

Kaolinite

The kaolinite density profiles show that ADONA molecules (dashed lines) are adsorbed near to the hydroxyl surface (Fig. 2b). The first carboxyl oxygen (O_1 and O_2) peaks are well-structured, and are located ~2.7 Å from the hydroxyl surface oxygens (oh), and are followed by a carboxyl carbon (C_{COO^-}) peak located at ~3 Å. The first density peak for the fluorine (F) atoms begins at ~3 Å from the basal surface, though more structured peaks are located at ~5.8 Å. The F peaks are aligned with peaks from the carbon backbone (C_{back}) beginning at ~4 Å. All other atoms of ADONA are observed beyond 5 Å, including both the ether oxygens and hydrogen (O_{eth1}, O_{eth2} and H), where peaks appear at distances ~5.5, 6.5, and 6.3 Å away from the surface, respectively. The presence of carboxyl groups closest to the surface indicate that the adsorption of ADONA on kaolinite is driven by the hydrogen bonding of carboxyl oxygen (O_1 and O_2) atoms with hydroxyl hydrogens (ho) of the aluminol surface. Notably, there are no interactions of ether oxygens or the fluorinated backbone with the kaolinite basal surface. Additionally, the ADP shows all atoms of ADONA molecules exist within 25 Å of the hydroxyl surface, while demonstrating a complete lack of ADONA interactions with the siloxane surface (Fig. 2c). Water exhibits different density distribution near either basal (aluminol/siloxane) that extends ~10 Å from the basal surfaces and can be attributed to the difference in hydrophilic/hydrophobic character inherent to the unique kaolinite basal surfaces. For example, Fig. 2b shows three peaks for oxygens of water (O_{H_2O}) located at ~2.5, 4.2 and 6.3 Å from the hydroxyl surface while the O_{H_2O} peaks near the siloxane surface are centered at ~2.6 Å followed by a broader peak distribution at ~6.4 Å. Lastly, Ca^{2+} are exclusively located near the siloxane surface between 129 and 132 Å, starting at ~4.5 Å (outer-sphere) from the basal surface oxygens (ob). The reported density distributions of water, Ca^{2+} and ADONA are consistent with our previous studies of carboxylate PFAS and kaolinite surfaces, thus indicating that the environmental distribution of ADONA may be similar to that of legacy and related ether-PFAS molecules.[18,41,66]

Montmorillonite

The ADONA molecules in the montmorillonite system show entirely different adsorption profiles, by including both surface adsorbed and solution phase cluster molecules. Fig. 2f shows the significant presence of F atoms at ~127.6 Å, or ~3 Å from the basal surface oxygen (ob) atoms. The H and F atoms on the ADONA backbone show the closest interaction with the surface which implies that the hydrophobic backbone plays a pivotal role in the surface complexation with montmorillonite. Both O_{eth1} and O_{eth2} are observed only at ~4.6 Å from the surface and hence are likely not responsible for adsorption. In contrast to the surface complexation observed in kaolinite, the presence of ADP peaks for the carboxyl group atoms at ~5.6 Å for C_{COO^-} and ~6.3 Å for O_1 and O_2 demonstrate that the hydrophilic headgroups do not participate in the surface complexation. In addition to surface adsorbed ADONA molecules, Fig. 2d shows that the ADONA molecules are distributed throughout the entire interparticle pore with peak densities at ~60 Å and ~111 Å. Such distribution indicates the potential for their aggregation within the bulk mesopore solution. Near surface interactions for O_{H_2O} are similar on either basal surface as shown in Fig. 2e and f, with three distinct peaks located at ~2.7, 4.5, and 6.3 Å from each basal surface, reaching bulk density beyond ~9 Å. Ca^{2+} shows two types of coordination (inner-

Open Access Article. Published on 13 October 2025. Downloaded on 10/26/2025 4:29:19 AM.
This article is licensed under a Creative Commons Attribution-NonCommercial 3.0 Unported Licence.

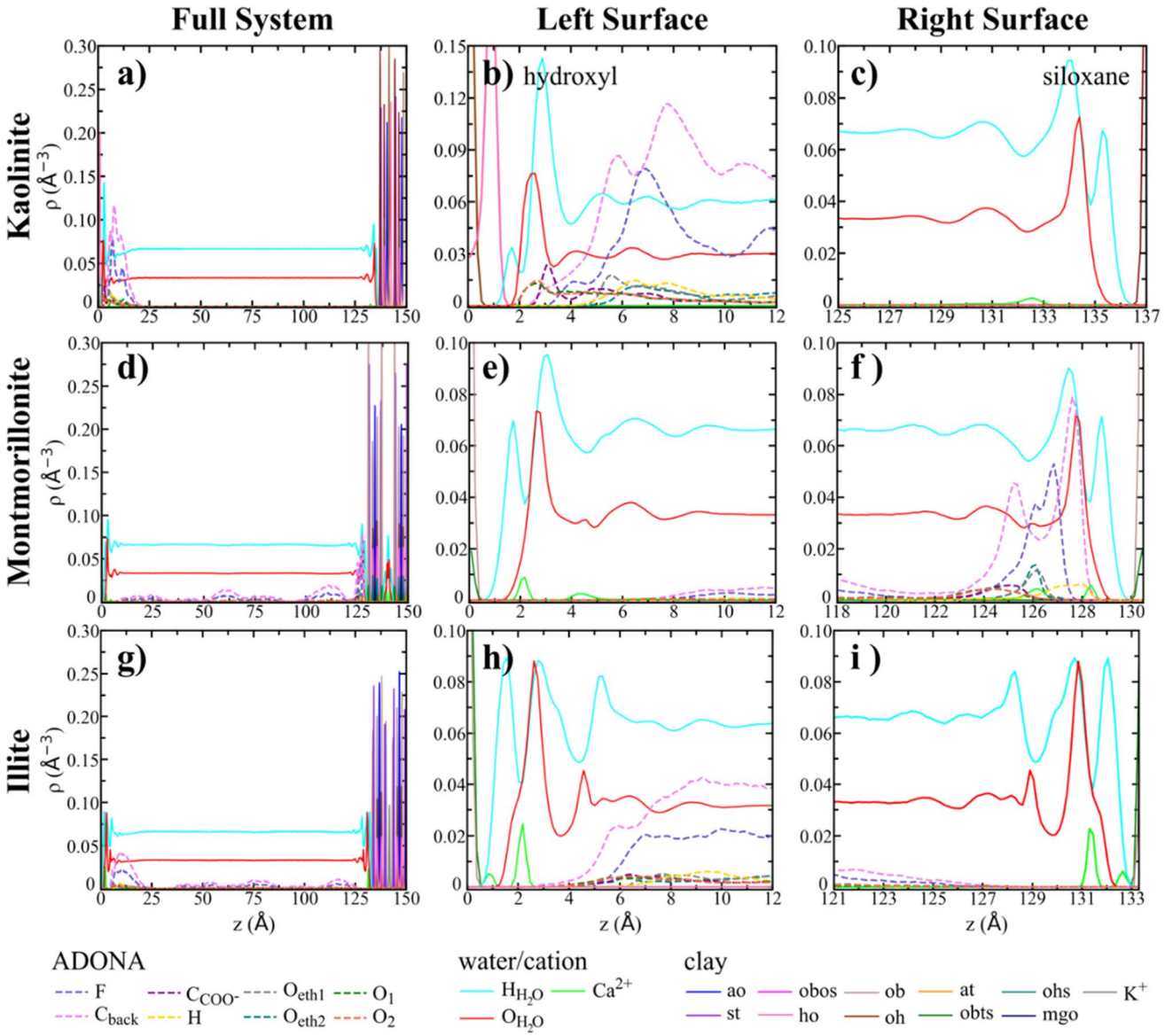

Fig. 2 ADPs of PFAS, cations and H_2O, computed for kaolinite (a–c), montmorillonite (d–f), and illite (g–i) with respect to the clay surface normal. For kaolinite, $z = 0$ represents the peak maximum of basal hydroxyl surface oxygen (oh) atoms and $z = 0$ is defined as the peak maximum of the basal surface tetrahedral oxygen (ob) atoms for montmorillonite and illite. The ADP's for the complete simulated systems (a, d and g), left surface interactions within ~12 Å (b, e and h), and right surface interactions within ~12 Å (c, f and i) are plotted. Color codes are shown at the bottom of the figure, where clay, water, and Ca^{2+} atom types are represented with solid lines, and ADONA atom types are represented with dashed lines. (All ADONA density peaks were increased ×20 to improve visibility).

sphere and outer-sphere) at ~2.1 Å and ~4.4 Å away from the basal surface of montmorillonite. Importantly, Ca^{2+} ions do not play a bridging role for the adsorption of ADONA at the montmorillonite surface and is similar to our previous Ca^{2+}-montmorillonite structures.[41] Thus, it is evident that the adsorption of carboxylate PFAS molecules with the montmorillonite surface are driven by the hydrophobic interaction between the basal surface atoms and the fluorinated backbone.[18,41]

Illite

Lastly, the illite system also shows an entirely unique influence on the density distribution of ADONA. Here, ADONA molecules are present exclusively in the bulk solution phase, as illustrated in Fig. 2g, and similar to the montmorillonite system. Unlike montmorillonite, there are particularly broad peaks for the F and C_{back} centered at ~10 Å within the interparticle pore, observed in Fig. 2g and h. This suggests that a larger aggregate may exist near the basal surface of illite. Evidently, there are more distinct water layers due to the charge distribution along the tetrahedral surface of illite. The first water layer is characterized by the small shoulder of water oxygens at ~2 Å, and is followed by five distinct peaks at ~2.6, 4.6, 5.4, 6.4, and 8.8 Å. Additionally, the Ca^{2+} shows two types of inner-sphere coordination with a small peak at ~0.8 Å (centered within the ditrigonal cavity) and a more intense peak at ~2.2 Å (located above a substituted Al^{3+} tetrahedra).

© 2025 The Author(s). Published by the Royal Society of Chemistry

Open Access Article. Published on 13 October 2025. Downloaded on 10/26/2025 4:29:19 AM.
This article is licensed under a Creative Commons Attribution-NonCommercial 3.0 Unported Licence.

Angle distribution of adsorbed ADONA

The orientation of all surface adsorbed ADONA species in kaolinite and montmorillonite were calculated relative to the basal surface normal of each clay model investigated. Note, the orientation of ADONA with the basal surfaces were determined only for surface adsorbed molecules corresponding to the first ADP peaks. Fig. 3a shows that the computed angle distributions of the carboxyl group are centered at ~130° with respect to the surface and corroborates that the carboxyl oxygen atoms of ADONA are oriented closest to hydroxyl surface of kaolinite. The broad peak extending from ~75° to ~180° demonstrates that the orientation of the carboxyl group can have either a single interacting oxygen, or both oxygens (O_1 and O_2) interacting simultaneously with hydroxyl hydrogen (ho) atoms. In tandem with the previous kaolinite-ADP discussion, the carboxyl groups of ADONA are oriented towards the surface while the backbone extends further into the solution phase, forming an interfacial structure that is similar to other PFAS that include carboxyl functionality, such as GenX, PFOA and PFBA.[41,66]

Since the ADPs for surface coordinated ADONA molecules in montmorillonite show that near surface interactions are dominated by the fluorinated backbone, the orientations were computed by considering the carbons on either end of the backbone (C_2–C_7) in ADONA, excluding the carboxyl group. The two distinct peaks shown in Fig. 3b indicate that the adsorbed ADONA molecules predominantly exist flat along the surface, responsible for a well-defined peak at ~90° along with a broader peak at ~110° with respect to the basal surface of montmorillonite. Such distribution depicts that the fluorinated backbone lies parallel, or near parallel, relative to the surface and is primarily due to the hydrophobic interactions dominate the adsorption between ADONA and montmorillonite. Furthermore, the broad peak in Fig. 3b extending to ~150° shows that the vector pointing towards C_7 on the backbone is oriented towards the surface. As a result, it follows that the functional groups bonded to C_2 (carboxyl's) of ADONA are located farthest away from the basal surface of montmorillonite, consistent with the reported ADP discussions.

Adsorption and coordination environments of ADONA

The impact of the clay surfaces on the complexation of ADONA at the interfacial regions are represented in Fig. 4a–f and S4–S6. Fig. 4a, b, and S4 show that all ADONA molecules are adsorbed at or near the hydroxyl surface of kaolinite. Consistent with other long-chain PFAS, ADONA tends to form large clusters (>5 molecules) at the surface.[66] Importantly, two large aggregates exist coordinated to the kaolinite surface through H-bonding: a hexamer (highlighted in orange) and a nonamer (highlighted in pink). Both clusters are (formed during the equilibration run of NVT ensemble) stable throughout the entire production run *via* the hydrophobic interaction between adjacent fluorinated backbones. On average, the nonamer exhibits one (but can have up to three) directly coordinated ADONA molecule that forms hydrogen bonds to the kaolinite surface. Similarly, the hexamer is coordinated to the surface *via* only one or two ADONA molecules at any given time. Both clusters are localized on the surface of kaolinite and hence do not show substantial lateral movement. The ADONA molecules in both clusters that are not directly in contact with the hydroxyl surface of kaolinite are highly dynamic within their aggregates. Notably, a single monomer exhibits transient coordination (association and dissociation with the surface at random time intervals) behavior with the hydroxyl surface during the data production run. The time averaged surface adsorbed aggregates of ADONA in kaolinite and montmorillonite are shown in Fig. S9.

As discussed in the ADP and angular distribution sections, the carboxyl groups are oriented towards the basal surface and interact directly with the octahedral hydroxyl hydrogen (ho) atoms of kaolinite. Fig. 5 highlights the two coordination environments of ADONA at the hydroxyl surface of kaolinite. For instance, Fig. 5a shows that one of the O_{COO^-} atoms of the carboxyl group of ADONA interacts with three surface hydroxyl groups at the center of a cavity. Fig. 5b demonstrates an interaction where both carboxyl oxygens are ~equidistant from the surface, and each oxygen interacts with separate hydroxyl groups on either end of an aluminol ring. Since the most prominent orientation is at ~130° (Fig. 3a), the configuration in

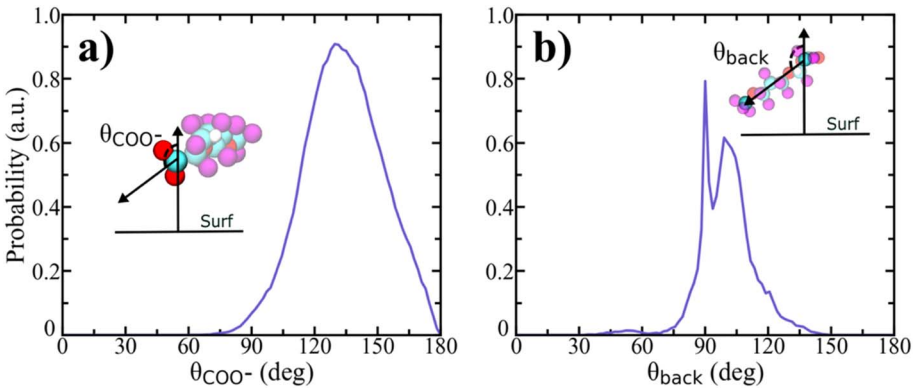

Fig. 3 Angle density distributions for adsorbed ADONA molecules to the basal (001) for the (a) kaolinite hydroxyl surface and (b) montmorillonite. For the kaolinite system, θ_{COO^-} corresponds to the bisecting angle of the vector of the carboxyl carbon (C_{COO^-}) to the center of the carboxyl oxygen atoms (O_1 and O_2) with respect to the surface normal. The montmorillonite θ_{back} angles correspond to the vector from C_2 to C_7 (terminal) with respect to the surface normal.

Open Access Article. Published on 13 October 2025. Downloaded on 10/26/2025 4:29:19 AM.
This article is licensed under a Creative Commons Attribution-NonCommercial 3.0 Unported Licence.

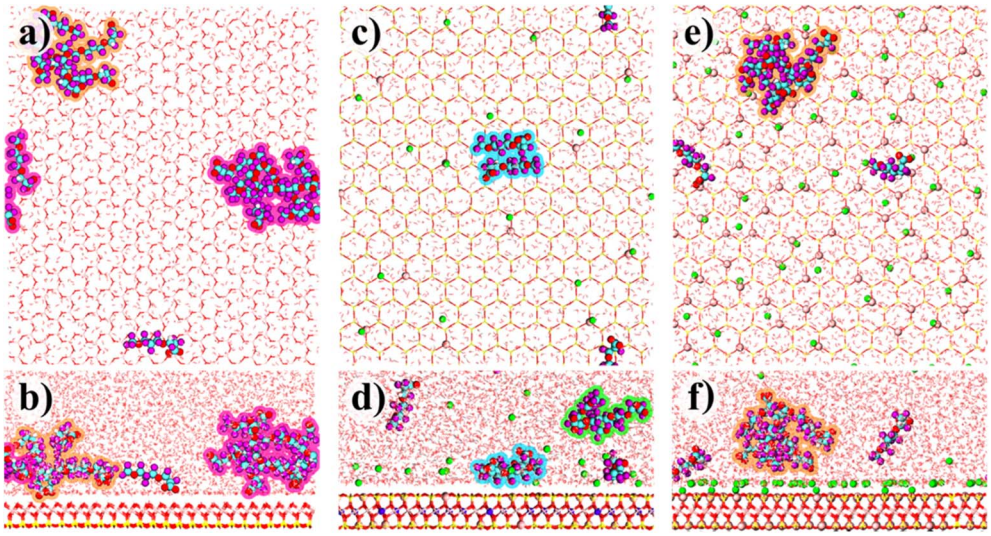

Fig. 4 Representative pictures of the external basal surface (001) adsorption and coordination environments of kaolinite (a and b), montmorillonite (c and d) and illite (e and f). Color codes: red sticks-surface O atoms; yellow sticks-Si; pink sticks-Al; pink spheres-substituted Al; blue spheres-substituted Mg; green spheres-Ca^{2+} ions; cyan spheres-C; purple spheres-F; red spheres-O; shaded red and white lines-H_2O; cyan highlight-dimer; green highlight-trimer; orange highlight-hexamer; pink highlight-nonamer.

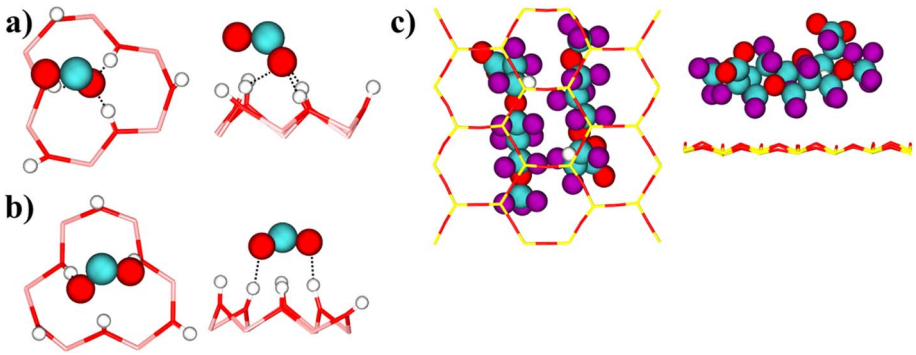

Fig. 5 Above planar and lateral view representation of the coordination environments of a single oxygen of a carboxyl group (a) and two oxygens of a carboxyl group (b) with the ditrigonal cavities of kaolinite on the hydroxyl surface. Montmorillonite surface (c) dimer interaction at the planar surface and a lateral view. Color codes: red sticks-O surface; pink sticks-Al octahedra; yellow sticks-Si; white spheres-H; red spheres-$O_{COO^-/eth}$; blue spheres-C; purple spheres-F. Note-carbon backbone is not shown to examine the carboxyl group interaction alone (a and b).

Fig. 5a is preferred rather than Fig. 5b and is the most prevalent coordination environment for the interaction of ADONA molecules with kaolinite.

In montmorillonite, two different surface adsorbed complexations of ADONA are observed: a single monomer interacting with the surface; and a dimer (blue highlight) that interacts with the hydrophobic areas on the basal surfaces of montmorillonite, as demonstrated in Fig. 4c, d and S5. For the adsorbed dimer species shown in Fig. 5c, the interaction between the hydrophobic backbone of ADONA and the hydrophobic regions between charged sites at the basal surface of montmorillonite is the dominating factor stabilizing the surface complexation, similar to other ether-PFAS like GenX with montmorillonite.[41] Notably, the dimer exists in antiparallel alignment between fluorinated backbones, where the terminal carboxyl groups are pointed in opposite directions (see Fig. 5c). The aliphatic H atoms for all surface adsorbed ADONA molecules are oriented towards the silicon tetrahedra. Fig. 5c further demonstrates that the ADONA 'H' atoms in the dimer are located directly above opposing silicon corners of the same ditrigonal cavity but also show some lateral movement along the surface. The reported interfacial structure of ADONA (H atoms closer to the basal surface) shows a key difference when compared to fluorotelomer FTC, that do not have H atoms oriented towards the surface.[18]

Non-surface bound clusters

Fig. 6 demonstrates that the ADONA molecules in the solution phase predominantly exist as monomeric units, along with highly stable aggregates varying in sizes for both montmorillonite and illite. The mesopore region in montmorillonite (Fig. 6a) shows that ~50% of the ADONA molecules exist as monomers, while the rest exist in two trimeric forms (green highlight). In illite, no surface adsorbed ADONA molecules are

© 2025 The Author(s). Published by the Royal Society of Chemistry

Open Access Article. Published on 13 October 2025. Downloaded on 10/26/2025 4:29:19 AM. This article is licensed under a Creative Commons Attribution-NonCommercial 3.0 Unported Licence.

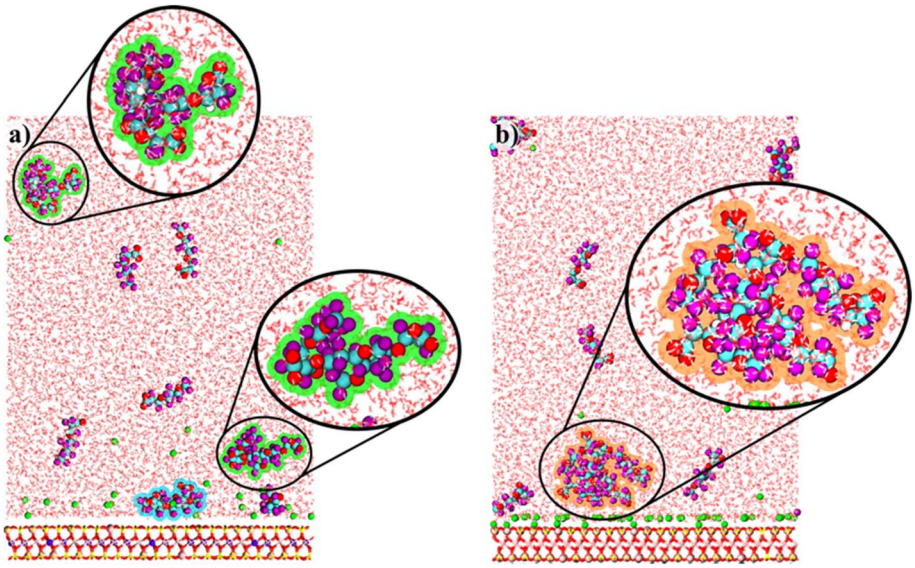

Fig. 6 Snapshots of the interparticle pore region for montmorillonite (a) and illite (b). Color codes: red sticks-surface O atoms; yellow sticks-Si; pink sticks-Al; pink spheres-substituted Al; blue spheres-substituted Mg; green spheres-Ca^{2+} ions; cyan spheres-C; purple spheres-F; red spheres-O; shaded red and white lines-H_2O; cyan highlight-dimer; green highlight-trimers; orange highlight-hexamer.

observed during the entire simulation run. For illite, ~60% of the ADONA molecules exist as monomers, while the rest exist in a hexameric unit (orange highlight) near the surface (Fig. 6b).

Radial distribution function

Radial distribution functions (RDF) were plotted to further validate the different coordination environments between ADONA molecules and the basal surface regions of each clay. RDFs were calculated to evaluate the mean interaction distances between key atomic pairs of ADONA atom types (F, H, ether oxygens: O_{eth}, carboxyl oxygens: O_{COO^-}) and the relevant basal surface atoms (H_{kaol}, O_{mont}, O_{illite}) described in the previous sections. Fig. 7 confirms that the adsorption of ADONA is entirely dependent on the clay surface.

Fig. 7a shows only one structured and well-defined peak that exists at ~1.8 Å for O_{COO^-}–H_{kaol} interaction with a running coordination number (RCN) of ~0.25. The remaining atom types of ADONA with H_{kaol} show diffuse peaks at distances >4 Å, and hence are not responsible for the coordination environments specific to the kaolinite surface. On the other hand, the presence of broad peaks for both F and H atoms of ADONA in montmorillonite justifies that the ADONA molecules are predominantly interacting with hydrophobic regions on the montmorillonite external surface *via* the fluorinated backbone and have the H atom factoring in atop silicon tetrahedra. Lastly, while the ADONA molecules displayed some proximity to the illite surface, Fig. 7c demonstrates that the absence of any stable or long-lasting coordination environments involving ADONA.

Diffusion of ADONA

Mean diffusion coefficients (D) were calculated for ADONA and water molecules in each clay system and are summarized in Fig. 8. Regardless of the mineral structure, the average diffusion of water is ~3.0×10^{-9} m^2 s^{-1} (see SI). All of the simulations show a significant decrease in mobility of ADONA by a factor of ~10 to 100 relative to water diffusion. The ADONA in the

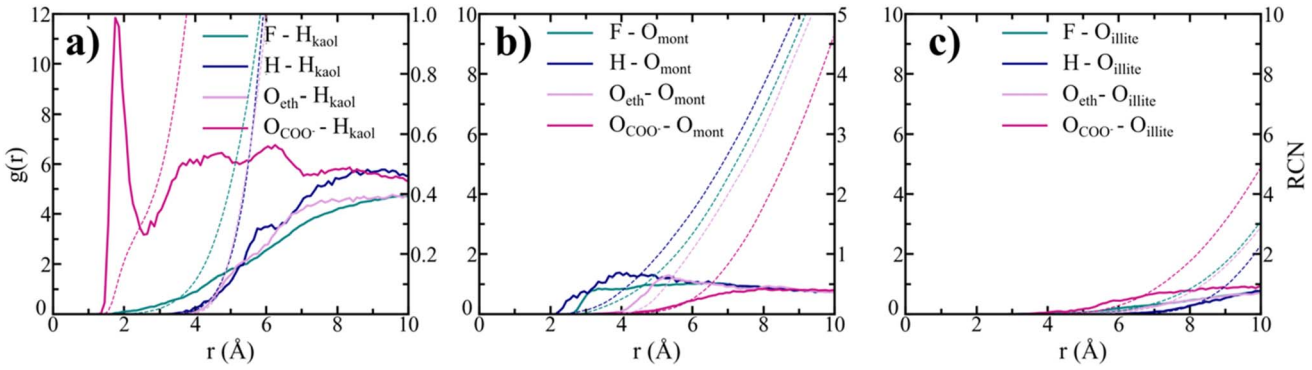

Fig. 7 Radial distribution function (solid lines) analysis and running coordination numbers (dashed lines) plots for ADONA interactions with kaolinite (a), montmorillonite (b) and illite (c).

Open Access Article. Published on 13 October 2025. Downloaded on 10/26/2025 4:29:19 AM. This article is licensed under a Creative Commons Attribution-NonCommercial 3.0 Unported Licence.

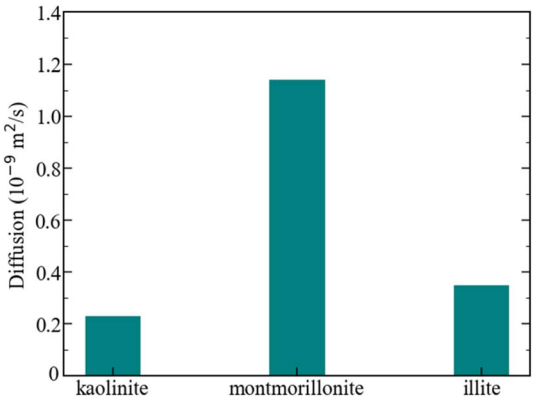

Fig. 8 Calculated average diffusion coefficients for ADONA molecules for each clay system. The uncertainties in the reported diffusion values are below 1%.

kaolinite external pore shows more restricted mobility with a diffusion value of ~0.23 × 10^{-9} m^2 s^{-1}. This can be attributed to the formation of larger aggregates that have minimal contact points associated directly to the kaolinite hydroxyl surface while the remaining ADONA molecules exist in a more mobile state. The ADONA molecules are dynamic within their respective aggregates, likely due to the reduced hydrophobicity resulting from the presence of additional ether linkages in the fluorinated backbone – an effect observed in other ether-PFAS and short-chain fluorocarbons.[41,66] Notably, the mean diffusion coefficients of ADONA in montmorillonite shows the highest diffusion of ~1.14 × 10^{-9} m^2 s^{-1}, which is attributed to the ADONA molecules largely existing as monomers in solution and also to only the small number of associated monomers and dimers at the surface. Finally, the diffusion of ADONA molecules in the illite system is greater than in kaolinite but lower than in montmorillonite and is most likely due to the formation of a large aggregate near the illitic surface. However, it is important to highlight that the diffusion of the surface adsorbed ADONA molecules with montmorillonite, irrespective of the complexation size, are substantially slower than the mean diffusion in illite (Table S2). The differences between the diffusion coefficients emphasizes the importance of mineral surfaces in dictating the mobility of ADONA molecules.

Conclusions

The interactions between ADONA, a replacement PFAS compound, and three distinct clay minerals were investigated using MD simulations under ambient thermodynamic conditions. The results reveal a strong dependence of ADONA's adsorption behavior on the structure and extent of the clay's structural charge, underscoring the critical role of mineralogical composition on PFAS transport in soil systems. Among the clays examined, ADONA exhibited the highest extent of adsorption to kaolinite, forming large, stable clusters that adhered to the surface through contact involving one to three molecules. The surface adsorption mechanism of ADONA on montmorillonite was similar to the observed for GenX, another ether-based PFAS.[41] In contrast, no direct adsorption of ADONA was observed at the illite basal surface. In general, the low or negligible direct adsorption of ADONA at the surfaces of minerals clearly indicates that the ether-based PFAS molecules prefer to be in the solution phase than at the surface, consistent with the sampling studies by Nguyen *et al.*[37]

Interestingly, the overall diffusion coefficients of ADONA in kaolinite and illite are relatively similar, though the three models show diffusion ranging from ~0.23–1.14 × 10^{-9} m^2 s^{-1}, several orders of magnitude lower than that of bulk water in the mesopores. These diffusion characteristics are indicative of hindered mobility which can attributed to a combination of factors, including coordination with the clay and the formation of ADONA aggregates of varying sizes within the pore space, which cause steric hindrance and restrict molecular motion.

These molecular-level observations carry significant implications for environmental systems. Soils dominated by neutral clays like kaolinite and montmorillonite may limit ADONA mobility through prolonged surface interactions, whereas illitic soils, which do not promote surface adsorption, may instead drive the ADONA molecules to aggregate within mesopores – ultimately lowering overall diffusion through self-assembly. Overall, this study emphasizes the importance of characterizing key soil mineral components to better predict the environment fate and mobility of emerging PFAS, informing more effective risk assessments and management practices. However, it is important to note that the interfacial adsorption characteristics are strongly influenced by pH, composition of PFAS matrices, nature of soil organic matter and should be carefully examined in future.

Conflicts of interest

There are no conflicts to declare.

Data availability

The data supporting this article have been included as part of the supplementary information (SI). Supplementary information: schematic of ADONA model atom types; average cell dimensions of clay systems post-NPT simulation; schematic of basal surfaces and internal octahedral sheets of clay systems; representation of initial simulation setup; schematic representations of the final clay system's simulation cells; ADP's of clay particles; water dipole orientations for clay systems; time-dependent surface adsorption schemes for kaolinite and montmorillonite; RDF's of Ca^{2+} in different environments, RDF's of water interactions with ADONA head group and backbone, water and cluster-dependent diffusion coefficients, and additional details about the simulation techniques and analysis. See DOI: https://doi.org/10.1039/d5va00243e. More information will be provided upon request.

Acknowledgements

This material is based upon work supported by the National Science Foundation under grant no. CHE-2107155. The authors

 © 2025 The Author(s). Published by the Royal Society of Chemistry

Open Access Article. Published on 13 October 2025. Downloaded on 10/26/2025 4:29:19 AM. This article is licensed under a Creative Commons Attribution-NonCommercial 3.0 Unported Licence.

also acknowledge computational resources from the National Energy Research Scientific Computing Center, which is supported by the Office of Science of the U.S. Department of Energy under ERCAP No. m1649 and m4306, and the ICER computational facility at Michigan State University.

References

1 Z. Wang, J. C. Dewitt, C. P. Higgins and I. T. Cousins, A Never-Ending Story of Per- and Polyfluoroalkyl Substances (PFASs)?, *Environ. Sci. Technol.*, 2017, **51**, 2508–2518.
2 R. C. Buck, J. Franklin, U. Berger, J. M. Conder, I. T. Cousins, P. De Voogt, A. A. Jensen, K. Kannan, S. A. Mabury and S. P. J. van Leeuwen, Perfluoroalkyl and polyfluoroalkyl substances in the environment: Terminology, classification, and origins, *Integr. Environ. Assess. Manage.*, 2011, **7**, 513–541.
3 E. M. Sunderland, X. C. Hu, C. Dassuncao, A. K. Tokranov, C. C. Wagner and J. G. Allen, A review of the pathways of human exposure to poly- and perfluoroalkyl substances (PFASs) and present understanding of health effects, *J. Expo. Sci. Environ. Epidemiol.*, 2019, **29**, 131–147.
4 N. Loganathan, C. E. Schumm, M. K. O'Reilly and A. K. Wilson, Adsorption and Dynamic Characteristics of PFAS Mixtures with Kaolinite: Molecular Insights into the Impact of Chain Length and Functional Group, *Environ. Sci. Technol.*, 2025, **59**, 14637–14648.
5 A. V. Shirke, E. G. Radke, C. Lin, R. Blain, N. Vetter, C. Lemeris, P. Hartman, H. Hubbard, M. Angrish, X. Arzuaga, J. Congleton, A. Davis, L. V. Dishaw, R. Jones, R. Judson, J. P. Kaiser, A. Kraft, L. Lizarraga, P. D. Noyes, G. Patlewicz, M. Taylor, A. J. Williams, K. A. Thayer and L. M. Carlson, Expanded Systematic Evidence Map for Hundreds of Per- and Polyfluoroalkyl Substances (PFAS) and Comprehensive PFAS Human Health Dashboard, *Environ. Health Perspect.*, 2024, **132**, 026001.
6 F. Coperchini, L. Croce, G. Ricci, F. Magri, M. Rotondi, M. Imbriani and L. Chiovato, *Thyroid Disrupting Effects of Old and New Generation PFAS*, Frontiers Media S.A, 2021, DOI: 10.3389/fendo.2020.612320.
7 T. T. Lai, Y. Eken and A. K. Wilson, Binding of Per- and Polyfluoroalkyl Substances to the Human Pregnane X Receptor, *Environ. Sci. Technol.*, 2020, **54**, 15986–15995.
8 E. C. Bonefeld-Jørgensen, M. Long, S. O. Fredslund, R. Bossi and J. Olsen, Breast cancer risk after exposure to perfluorinated compounds in Danish women: a case–control study nested in the Danish National Birth Cohort, *Cancer Causes Control*, 2014, **25**, 1439–1448.
9 Z. Wang, A. M. Buser, I. T. Cousins, S. Demattio, W. Drost, O. Johansson, K. Ohno, G. Patlewicz, A. M. Richard, G. W. Walker, G. S. White and E. Leinala, A New OECD Definition for Per- and Polyfluoroalkyl Substances, *Environ. Sci. Technol.*, 2021, **55**, 15575–15578.
10 C. F. Kwiatkowski, D. Q. Andrews, L. S. Birnbaum, T. A. Bruton, J. C. DeWitt, D. R. U. Knappe, M. V. Maffini, M. F. Miller, K. E. Pelch, A. Reade, A. Soehl, X. Trier, M. Venier, C. C. Wagner, Z. Wang and A. Blum, Scientific Basis for Managing PFAS as a Chemical Class, *Environ. Sci. Technol. Lett.*, 2020, **7**, 532–543.
11 J. C. Biffinger, H. W. Kim and S. G. DiMagno, The Polar Hydrophobicity of Fluorinated Compounds, *ChemBioChem*, 2004, **5**, 622–627.
12 B. E. Smart, Fluorine substituent effects (on bioactivity), *J. Fluor. Chem.*, 2001, **109**, 3–11.
13 M. P. Krafft and J. G. Riess, Per- and polyfluorinated substances (PFASs): Environmental challenges, *Curr. Opin. Colloid Interface Sci.*, 2015, **20**, 192–212.
14 T. R. L. Melin, P. Harell, B. Ali, N. Loganathan and A. K. Wilson, Thermochemistry of per- and polyfluoroalkyl substances, *J. Comput. Chem.*, 2023, **44**, 570–580.
15 K. Sznajder-Katarzyńska, M. Surma and I. Cieślik, A Review of Perfluoroalkyl Acids (PFAAs) in terms of Sources, Applications, Human Exposure, Dietary Intake, Toxicity, Legal Regulation, and Methods of Determination, *J. Chem.*, 2019, **2019**, 1–20.
16 L. Ahrens and M. Bundschuh, Fate and effects of poly- and perfluoroalkyl substances in the aquatic environment: A review, *Environ. Toxicol. Chem.*, 2014, **33**, 1921–1929.
17 L. Ahrens, Polyfluoroalkyl compounds in the aquatic environment: A review of their occurrence and fate, *J. Environ. Monit.*, 2011, **13**, 20–31.
18 N. Loganathan, L. Ashby, C. E. Schumm and A. K. Wilson, Interfacial adsorption and dynamics of fluorotelomers with soil minerals – mechanistic insights, *Environ. Sci. Nano*, 2025, **12**, 850–862.
19 G. Munoz, J. Liu, S. Vo Duy and S. Sauvé, Analysis of F-53B, Gen-X, ADONA, and emerging fluoroalkylether substances in environmental and biomonitoring samples: A review, *Trends Environ. Anal. Chem.*, 2019, **23**, e00066.
20 S. Wang, J. Huang, Y. Yang, Y. Hui, Y. Ge, T. Larssen, G. Yu, S. Deng, B. Wang and C. Harman, First Report of a Chinese PFOS Alternative Overlooked for 30 Years: Its Toxicity, Persistence, and Presence in the Environment, *Environ. Sci. Technol.*, 2013, **47**, 10163–10170.
21 P. A. Rice, J. Cooper, S. E. Koh-Fallet and S. V. Kabadi, Comparative analysis of the physicochemical, toxicokinetic, and toxicological properties of ether-PFAS, *Toxicol. Appl. Pharmacol.*, 2021, **422**, 115531.
22 M. J. Bentel, Y. Yu, L. Xu, H. Kwon, Z. Li, B. M. Wong, Y. Men and J. Liu, Degradation of Perfluoroalkyl Ether Carboxylic Acids with Hydrated Electrons: Structure–Reactivity Relationships and Environmental Implications, *Environ. Sci. Technol.*, 2020, **54**, 2489–2499.
23 S. Feng, X. Lu, K. Ouyang, G. Su, Q. Li, B. Shi and J. Meng, Environmental occurrence, bioaccumulation and human risks of emerging fluoroalkylether substances: Insight into security of alternatives, *Sci. Total Environ.*, 2024, **922**, 171151.
24 S. C. Gordon, Toxicological evaluation of ammonium 4,8-dioxa-3H-perfluorononanoate, a new emulsifier to replace ammonium perfluorooctanoate in fluoropolymer manufacturing, *Regul. Toxicol. Pharmacol.*, 2011, **59**, 64–80.
25 M. Schlummer, C. Sölch, T. Meisel, M. Still, L. Gruber and G. Wolz, Emission of perfluoroalkyl carboxylic acids (PFCA) from heated surfaces made of polytetrafluoroethylene

Open Access Article. Published on 13 October 2025. Downloaded on 10/26/2025 4:29:19 AM. This article is licensed under a Creative Commons Attribution-NonCommercial 3.0 Unported Licence.

(PTFE) applied in food contact materials and consumer products, *Chemosphere*, 2015, **129**, 46–53.
26 R. Mueller and K. E. Schlosser, *History and Use of Per- and Polyfluoroalkyl Substances (PFAS) Found in the Environment*, Washington DC, 2020.
27 B. Tansel, *PFAS Use in Electronic Products and Exposure Risks during Handling and Processing of E-Waste: A Review*, Academic Press, 2022, DOI: 10.1016/j.jenvman.2022.115291.
28 F. Heydebreck, J. Tang, Z. Xie and R. Ebinghaus, Alternative and Legacy Perfluoroalkyl Substances: Differences between European and Chinese River/Estuary Systems, *Environ. Sci. Technol.*, 2015, **49**, 8386–8395.
29 T. Gonaus, *Identifikation der Herkunft ausgewählter PFAS im Donaueinzugsgebiet oberhalb von Wien Identification of the origin of selected PFAS in the Danube catchment above Vienna of Civil and Environmental Engineering*, 2023.
30 B. Guo, J. Zeng, M. L. Brusseau and Y. Zhang, A screening model for quantifying PFAS leaching in the vadose zone and mass discharge to groundwater, *Adv. Water Resour.*, 2022, **160**, 104102.
31 Y. Tian, C. Xu, L. Zhang, D. Shi, F. Cappelli and S. Yin, Maternal Exposure to Per- and Polyfluoroalkyl Substances: Implications for Intrahepatic Cholestasis of Pregnancy and Adverse Birth Outcomes, *Exposure Health*, 2024, **16**, 1209–1223.
32 H. Fromme, M. Wöckner, E. Roscher and W. Völkel, ADONA and perfluoroalkylated substances in plasma samples of German blood donors living in South Germany, *Int. J. Hyg. Environ. Health*, 2017, **220**, 455–460.
33 R. Awad, Y. Zhou, E. Nyberg, S. Namazkar, W. Yongning, Q. Xiao, Y. Sun, Z. Zhu, Å. Bergman and J. P. Benskin, Emerging per- and polyfluoroalkyl substances (PFAS) in human milk from Sweden and China, *Environ. Sci.:Processes Impacts*, 2020, **22**, 2023–2030.
34 M. Kotthoff, A. Fliedner, H. Rüdel, B. Göckener, M. Bücking, A. Biegel-Engler and J. Koschorreck, Per- and polyfluoroalkyl substances in the German environment – Levels and patterns in different matrices, *Sci. Total Environ.*, 2020, **740**, 140116.
35 Y. Cheng, Q. An, H. Qi, R. Li, W. Liu, B. Gu and K. Liu, Temporal Trends of Legacy and Emerging PFASs from 2011 to 2021 in Agricultural Soils of Eastern China: Impacts of the Stockholm Convention, *Environ. Sci. Technol.*, 2023, **57**, 9277–9286.
36 A. Biegel-Engler and J. Frauenstein, *PFAS in Soil and Groundwater: Comprehensive Challenges and Progress in Regulation and Management in Germany*, 2024, pp. 285–304.
37 T. M. H. Nguyen, J. Bräunig, K. Thompson, J. Thompson, S. Kabiri, D. A. Navarro, R. S. Kookana, C. Grimison, C. M. Barnes, C. P. Higgins, M. J. McLaughlin and J. F. Mueller, Influences of Chemical Properties, Soil Properties, and Solution pH on Soil–Water Partitioning Coefficients of Per- and Polyfluoroalkyl Substances (PFASs), *Environ. Sci. Technol.*, 2020, **54**, 15883–15892.
38 R. S. Kookana, D. A. Navarro, S. Kabiri and M. J. McLaughlin, Key properties governing sorption–desorption behaviour of poly- and perfluoroalkyl substances in saturated and unsaturated soils: a review, *Soil Res.*, 2022, **61**, 107–125.
39 W. Cai, D. A. Navarro, J. Du, G. Ying, B. Yang, M. J. McLaughlin and R. S. Kookana, Increasing ionic strength and valency of cations enhance sorption through hydrophobic interactions of PFAS with soil surfaces, *Sci. Total Environ.*, 2022, **817**, 152975.
40 Y. Li, D. P. Oliver and R. S. Kookana, A critical analysis of published data to discern the role of soil and sediment properties in determining sorption of per and polyfluoroalkyl substances (PFASs), *Sci. Total Environ.*, 2018, **628–629**, 110–120.
41 C. E. Schumm, N. Loganathan and A. K. Wilson, Influence of Soil Minerals on the Adsorption, Structure, and Dynamics of GenX, *ACS ES&T Water*, 2023, **3**, 2659–2670.
42 R. T. Cygan, J. J. Liang and A. G. Kalinichev, Molecular models of hydroxide, oxyhydroxide, and clay phases and the development of a general force field, *J. Phys. Chem. B*, 2004, **108**, 1255–1266.
43 B. F. Ngouana W. and A. G. Kalinichev, Structural arrangements of isomorphic substitutions in smectites: Molecular simulation of the swelling properties, interlayer structure, and dynamics of hydrated cs-montmorillonite revisited with new clay models, *J. Phys. Chem. C*, 2014, **118**, 12758–12773.
44 S. P. Altaner, C. A. Weiss and R. J. Kirkpatrick, Evidence from 29Si NMR for the structure of mixed-layer illite/smectite clay minerals, *Nature*, 1988, **331**, 699–702.
45 W. Lowenstein, *Max Lowenstein*, Mineralogical Society of America, São Paulo, 1954.
46 J. Jia, D. Wu, J. Lin and X. Jiang, Molecular dynamics simulation of illite: From particle associations to hydration properties, *Appl. Clay Sci.*, 2023, **234**, 106850.
47 E. V. Tararushkin, V. V. Pisarev and A. G. Kalinichev, Atomistic simulations of ettringite and its aqueous interfaces: Structure and properties revisited with the modified ClayFF force field, *Cem. Concr. Res.*, 2022, **156**, 106759.
48 J. A. R. Willemsen, M. Emunah and I. C. Bourg, Molecular dynamics simulation of organic contaminant adsorption on organic-coated smectite clay, *Soil Sci. Soc. Am. J.*, 2022, **86**, 238–252.
49 H. T. Nguyen and M. T. Nguyen, Effects of Water Molecules on Rearrangements of Formamide on the Kaolinite Basal (001) Surface, *J. Phys. Chem. A*, 2014, **118**, 7017–7023.
50 M. H. Anvari and P. Choi, Salt-Induced Phase Separation of Water and Cyclohexane within a Kaolinite Nanopore: A Molecular Dynamics Study, *J. Phys. Chem. C*, 2018, **122**, 24215–24225.
51 W. A. Gebbink and S. P. J. van Leeuwen, *Environmental Contamination and Human Exposure to PFASs Near a Fluorochemical Production Plant: Review of Historic and Current PFOA and GenX Contamination in the Netherlands*, Elsevier Ltd, 2020, vol. 137, p. 105583.
52 J. J. Ellington, J. W. Washington, J. J. Evans, T. M. Jenkins, S. C. Hafner and M. P. Neill, Analysis of fluorotelomer

 © 2025 The Author(s). Published by the Royal Society of Chemistry

Open Access Article. Published on 13 October 2025. Downloaded on 10/26/2025 4:29:19 AM.
This article is licensed under a Creative Commons Attribution-NonCommercial 3.0 Unported Licence.

alcohols in soils: Optimization of extraction and chromatography, *J. Chromatogr. A*, 2009, **1216**, 5347–5354.
53 S. Plimpton, Fast Parallel Algorithms for Short-Range Molecular Dynamics, *J. Comput. Phys.*, 1995, **117**, 1–19.
54 W. Shinoda, M. Shiga and M. Mikami, Rapid estimation of elastic constants by molecular dynamics simulation under constant stress, *Phys. Rev. B: Condens. Matter Mater. Phys.*, 2004, **69**, 134103.
55 M. E. Tuckerman, J. Alejandre, R. López-Rendón, A. L. Jochim and G. J. Martyna, A Liouville-operator derived measure-preserving integrator for molecular dynamics simulations in the isothermal-isobaric ensemble, *J. Phys. A:Math. Gen.*, 2006, **39**, 5629–5651.
56 O. Teleman, B. Jönsson and S. Engström, A molecular dynamics simulation of a water model with intramolecular degrees of freedom, *Mol. Phys.*, 1987, **60**, 193–203.
57 W. D. Cornell, P. Cieplak, C. I. Bayly, I. R. Gould, K. M. Merz, D. M. Ferguson, D. C. Spellmeyer, T. Fox, J. W. Caldwell and P. A. Kollman, A Second Generation Force Field for the Simulation of Proteins, Nucleic Acids, and Organic Molecules, *J. Amer. Chem. Soc.*, 1995, **117**, 5179–5197.
58 A. Jakalian, D. B. Jack and C. I. Bayly, Fast, efficient generation of high-quality atomic charges. AM1-BCC model: II. Parameterization and validation, *J. Comput. Chem.*, 2002, **23**, 1623–1641.
59 J. Wang, W. Wang, P. A. Kollman and D. A. Case, Automatic atom type and bond type perception in molecular mechanical calculations, *J. Mol. Graphics Modell.*, 2006, **25**, 247–260.
60 J. A. Greathouse, D. B. Hart, G. M. Bowers, R. J. Kirkpatrick and R. T. Cygan, Molecular Simulation of Structure and Diffusion at Smectite–Water Interfaces: Using Expanded Clay Interlayers as Model Nanopores, *J. Phys. Chem. C*, 2015, **119**, 17126–17136.
61 C. M. Luft, T. C. Schutt and M. K. Shukla, Properties and Mechanisms for PFAS Adsorption to Aqueous Clay and Humic Soil Components, *Environ. Sci. Technol.*, 2022, **56**, 10053–10061.
62 N. Loganathan, B. O. Ferguson, B. Arey, H. E. Argersinger and G. M. Bowers, A Mechanistic Exploration of Natural Organic Matter Aggregation and Surface Complexation in Smectite Mesopores, *J. Phys. Chem. A*, 2020, **124**, 9832–9843.
63 N. Loganathan, A. O. Yazaydin, G. M. Bowers, A. G. Kalinichev and R. J. Kirkpatrick, Cation and Water Structure, Dynamics, and Energetics in Smectite Clays: A Molecular Dynamics Study of Ca–Hectorite, *J. Phys. Chem. C*, 2016, **120**, 12429–12439.
64 J. A. R. Willemsen and I. C. Bourg, Molecular dynamics simulation of the adsorption of per- and polyfluoroalkyl substances (PFASs) on smectite clay, *J. Colloid Interface Sci.*, 2021, **585**, 337–346.
65 S. Plimpton, R. Pollock and M. Stevens, *Proceedings of the Eighth {SIAM} Conference on Parallel Processing for Scientific Computing*, SIAM, Minneapolis, 1997.
66 N. Loganathan and A. K. Wilson, Adsorption, Structure, and Dynamics of Short- and Long-Chain PFAS Molecules in Kaolinite: Molecular-Level Insights, *Environ. Sci. Technol.*, 2022, **56**, 8043–8052.